

HistoPerm: A Permutation-Based View Generation Approach for Learning Histopathologic Feature Representations

Joseph DiPalma, Lorenzo Torresani, and Saeed Hassanpour

Abstract— Recently, deep learning methods have been successfully applied to solve numerous challenges in the field of digital pathology. However, many of these approaches are fully supervised and require annotated images. Annotating a histology image is a time-consuming and tedious process for even a highly skilled pathologist, and, as such, most histology datasets lack region-of-interest annotations and are weakly labeled. In this paper, we introduce HistoPerm, a view generation approach designed for improving the performance of representation learning techniques on histology images in weakly supervised settings. In HistoPerm, we permute augmented views of patches generated from whole-slide histology images to improve classification accuracy. These permuted views belong to the same original slide-level class but are produced from distinct patch instances. We tested adding HistoPerm to BYOL and SimCLR, two prominent representation learning methods, on two public histology datasets for Celiac disease and Renal Cell Carcinoma. For both datasets, we found improved performance in terms of accuracy, F1-score, and AUC compared to the standard BYOL and SimCLR approaches. Particularly, in a linear evaluation configuration, HistoPerm increases classification accuracy on the Celiac disease dataset by 8% for BYOL and 3% for SimCLR. Similarly, with HistoPerm, classification accuracy increases by 2% for BYOL and 0.25% for SimCLR on the Renal Cell Carcinoma dataset. The proposed permutation-based view generation approach can be adopted in common representation learning frameworks to capture histopathology features in weakly supervised settings and can lead to whole-slide classification outcomes that are close to, or even better than, fully supervised methods.

Index Terms— Deep neural networks, Digital pathology, Representation learning

Manuscript received September 4, 2022. (Corresponding author: Saeed Hassanpour.)

This research was supported in part by grants from the US National Library of Medicine (R01LM012837 and R01LM013833) and the US National Cancer Institute (R01CA249758).

Joseph DiPalma and Lorenzo Torresani are with the Department of Computer Science at Dartmouth College, Hanover, NH 03755 USA (email: joseph.r.dipalma.gr@dartmouth.edu; lt@dartmouth.edu).

Saeed Hassanpour is with the Department of Computer Science at Dartmouth College, Hanover, NH 03755 USA and the Departments of Biomedical Data Science and Epidemiology at Geisel School of Medicine at Dartmouth, Hanover, NH 03755 USA (email: saeed.hassanpour@dartmouth.edu).

I. INTRODUCTION

DIGITAL pathology is a relatively new field built around visualizing whole-slide images to aid pathologists in disease diagnosis. Whole-slide images, or WSIs, are scanned and digitized at high resolutions (up to $150,000 \times 150,000$ pixels) and then manually reviewed or analyzed using computational tools. Digitizing the WSIs removes the need for microscopic inspection but introduces a myriad of issues due to the massive gigapixel size of these images.

Computer vision-based methods and solutions have been developed for various applications in the digital pathology domain in recent years [1]–[8]. Of note, traditional supervised computer vision tasks on natural images differ from WSIs in three key ways: 1) the labeling process requires highly trained experts, while natural images tend to require no or minimal prerequisites for labeling; 2) labels are typically provided at the slide level; 3) the class label may only be determined by a small portion of the WSI. Of these issues, the second and third are mostly unique to histology images. Due to the large size of the WSIs, it is infeasible for pathologists to label all sections of a slide. Instead, the label is usually provided at the slide level, which also encompasses class-negative regions of the slide. Moreover, an object in the average image from the ImageNet natural image dataset occupies 25% of the area [9], while a typical “object” (i.e., region-of-interest annotation) in a WSI can occupy less than 15% [10]. The combination of weak labeling and low object scale poses a unique challenge and makes applying standard computer vision methods a sub-optimal solution in digital pathology. Given that a typical WSI is at least $30,000 \times 30,000$ pixels in size at $20\times$ magnification (0.5 $\mu\text{m}/\text{pixel}$), most works necessitate the preprocessing of these images into small patches (typically 224×224 pixels) for efficient processing. While conversion to patches makes running deep learning models easier, it can lead to further problems if the weakly labeled nature of the slides is not considered. Several recent works have proposed solutions to this problem by using techniques such as multiple-instance learning [11], [12], while others have focused on addressing the computational cost issue [13], [14]. In this work, we opted to use 224×224 -pixel patches and propose a model-agnostic view generation solution to capture histopathologic features more effectively with representation learning for WSI classification.

To address the challenges of histology image classification, we build upon recent advancements in self-supervised representation learning, namely, BYOL [15] and SimCLR [16], [17], to exploit the unique characteristics of weakly labeled histology images. Both BYOL and SimCLR belong to a leading class of self-supervised representation learning methods named Siamese representation learning due to their operation on two or more input views. Siamese network architectures utilize either weight-sharing (i.e., SimCLR [16], SimSiam [18]) or momentum encoders (i.e., BYOL [15], MoCo [19]) to learn representations of the latent space across multiple input views. We take advantage of these advancements in Siamese networks and propose our method, HistoPerm, to provide improved performance on histology images in representation learning scenarios.

Whereas prior approaches for histology image classification have used either the entire slide, a patch-aggregation method, or a combination, we avoid these workarounds entirely and utilize the weakly labeled nature of these images. As each patch may not be indicative of the slide-level label (i.e., be class-positive), we perform a permutation on a portion of the mini-batch where the view comes from the same class but a different instance of the class. Due to the low occurrence of class-positive patches in each WSI, we can leverage the large, combined pool of class-positive and class-negative patches to build stronger representations in the model. In WSIs, many of the patches are effectively interchangeable (i.e., permutable) due in part to the low ratio of class-positive to negative patches in addition to the lack of distinct visual attributes. Additionally, prior works have shown that representation learning approaches rely on building representations that are invariant to irrelevant variations in the input [20]. In this work, we utilize the fact that a typical patch from a WSI is class-negative in order to interpret the rest of the patches from the slide as being potential candidates for enforcing invariance to irrelevant features. Furthermore, we allow for permutation at the mini-batch scale with the assumption that this invariance holds across all, or at least the vast majority of, weakly labeled slides in a class. While we can still encounter instances where class-positive and class-negative instances are paired, these cases are not common enough to prevent feature learning, and as shown in prior works [21], such hard examples may even prove beneficial to learning. Moreover, HistoPerm is model-agnostic and can be integrated into any Siamese representation learning framework operating on two input views to learn better histopathologic feature representations when compared to the standard versions.

II. RELATED WORK

A. Self-supervised Representation Learning

Self-supervised representation learning techniques have made great strides in recent years in solving outstanding problems in computer vision. Self-supervised methods use a pretext task to learn a latent representation of an unlabeled dataset. As unlabeled datasets are easy to obtain in most domains, this allows for learning better representations without requiring labor-intensive manually-labeled datasets. Initial pretext tasks

were simplistic and involved undoing an augmentation of the input data, such as colorization [22], [23], rotation [24], [25], jigsaw [26], or counting [27]. However, more recent representation learning techniques have become increasingly complex and rely on methods such as contrastive learning [16], [17], [19], [21], [28]–[31], clustering [32]–[34], noncontrastive learning [15], [18], [35], and information preservation [36]–[38].

Contrastive approaches rely on positive and negative samples to “attract” and “repel” each other to guide the network by learning unique identifiers for each class in the downstream task. Unfortunately, the loss formulation in contrastive learning frameworks necessitates large mini-batch sizes (> 256) among other implementation details to produce high-quality latent representations. Smaller mini-batch sizes can be used by implementing “tricks” such as momentum encoders [19], [28], but in general, these approaches are still resource intensive and require massive computational power that is inaccessible to most researchers.

Existing clustering-based methods either use iterative cluster pseudolabeling [32], [33] or a variant of contrastive learning [34]. Either version relies on forcing differing sample embeddings to map to different clusters. A benefit of clustering approaches, even contrastive ones, is that they work well on smaller mini-batch sizes so they can be used in computationally or memory-constrained situations.

In contrast, noncontrastive approaches (i.e., using only positive instances) are much less memory- and computationally-intensive and can operate on smaller mini-batch sizes, albeit with a slight classification metric performance reduction in comparison to larger mini-batch sizes [15], [18], [35]. The underlying principle that prevents convergence to trivial, constant (i.e., collapsed) embeddings in these methods is unknown, but prior works have shown that implementation details do at least play some part in their success [18], [39], [40].

Finally, information preservation methods operate by decorrelating each pair of variables in the embeddings [36]–[38]. Unlike other self-supervised schemes, information preservation methods are explicitly designed to avoid collapse. The proposed Barlow Twins method optimizes the cross-correlation between embeddings and pushes it to the identity matrix. Similarly, Whitening-MSE (W-MSE) constrains the embeddings to lie on a spherical distribution, which is equivalent to enforcing an identity matrix for covariance [37]. Furthermore, VICReg is a generalized form of the Barlow Twins method, as it incorporates the same covariance constraint but adds additional terms for variance and invariance.

B. Histology Image Classification

Several approaches have been proposed for histology image classification in digital pathology. Commonly, large whole-slide images are converted to fixed-size smaller patches, and then a convolutional neural network is used for patch classification [1], [3]–[5], [41]–[44]. The patch classification results are then aggregated for whole-slide inferencing. In recent years, more complex approaches involving attention [2], [45] or multiple-instance learning (MIL) [46]–[54] have become widespread. Attention- or MIL-based methods match the

weakly labeled nature of histology images but still necessitate large, labeled datasets.

To address the bottleneck of access to large, labeled datasets, self-supervision has been successfully applied to histology images using existing computer vision methods [55]–[59]. These approaches aim to exploit unique characteristics of histology images, such as rotation invariance or local-to-global consistency. Contrastive learning-based methods have also become increasingly prevalent in histology feature representation [11], [12], [60]–[65]. Contrastive Predictive Coding (CPC) has proven to be a popular choice for contrastive histology methods, as the sliding window-like application is analogous to how pathologists examine portions of slides under a microscope [11], [62]. Similarly, methods such as DSMIL use SimCLR in a histology-appropriate fashion to incorporate multiscale information into contrastive models [12].

III. METHOD

In this section, we introduce our proposed method, HistoPerm, a permutation-based view generation method to improve capturing histopathologic features in representation learning frameworks.

A. WSI to Patch Conversion

Let \mathcal{D} be a dataset comprised of WSIs. Disjoint labeled and unlabeled subsets \mathcal{D}_l and \mathcal{D}_u partition \mathcal{D} . For each WSI $\mathcal{S}_i \in \mathcal{D}_l$, we have an associated ground-truth label y_i corresponding to the pathologist-provided slide-level classification label. Given a slide \mathcal{S}_i , we produce a set of patches p_i and assign them the slide-level label y_i . Weak labeling means we can have anywhere between 1 and $|p_i|$ class-positive patches per set p_i . As stated earlier, in general, we can assume that the majority of patches in p_i will be negative relative to slide-level class y_i . However, this is not problematic, as we do not wish to learn the class-decision boundaries explicitly in this stage but rather the underlying representation space. As a byproduct, we expect this representation space to be representative of features needed for the downstream classification. After this step, we have labeled and unlabeled sets of patches \mathcal{P}_l and \mathcal{P}_u produced from \mathcal{D}_l and \mathcal{D}_u , respectively. In the next section, we explain how we generate the input views for our model, given \mathcal{P}_l and \mathcal{P}_u .

B. View Generation

View Augmentation: Given a labeled patch dataset \mathcal{P}_l and unlabeled patch dataset \mathcal{P}_u , we randomly sample mini-batches \mathcal{X}_l and \mathcal{X}_u such that $\mathcal{X}_l \sim \mathcal{P}_l$ and $\mathcal{X}_u \sim \mathcal{P}_u$. Starting with sets of data transformations \mathcal{T}_1 and \mathcal{T}_2 , we compute $x_{u,i}^{(1)} = t_1(x_{u,i})$ and $x_{u,i}^{(2)} = t_2(x_{u,i})$ with $t_1 \sim \mathcal{T}_1$ and $t_2 \sim \mathcal{T}_2$ for all $x_{u,i} \in \mathcal{X}_u$. These augmented instances are combined to form views $v_{u,1} = \{x_{u,1}^{(1)}, x_{u,2}^{(1)}, \dots, x_{u,|\mathcal{X}_u|}^{(1)}\}$ and $v_{u,2} = \{x_{u,1}^{(2)}, x_{u,2}^{(2)}, \dots, x_{u,|\mathcal{X}_u|}^{(2)}\}$. Analogously, we produce augmented views of the labeled mini-batch \mathcal{X}_l , denoted as $v_{l,1} = \{x_{l,1}^{(1)}, x_{l,2}^{(1)}, \dots, x_{l,|\mathcal{X}_l|}^{(1)}\}$ and $v_{l,2} = \{x_{l,1}^{(2)}, x_{l,2}^{(2)}, \dots, x_{l,|\mathcal{X}_l|}^{(2)}\}$. Next, we describe our view permutation process on labeled views $v_{l,1}$ and $v_{l,2}$.

View Permutation: Given labeled augmented views, $v_{l,1}$ and $v_{l,2}$, we define a bijective permutation function $\pi : \{1, \dots, |\mathcal{X}_l|\} \rightarrow \{1, \dots, |\mathcal{X}_l|\}$ to generate a random permutation of $v_{l,1}$ denoted as $\widetilde{v_{l,1}}$. Our permuted view, $\widetilde{v_{l,1}}$, is defined as

$$\widetilde{v_{l,1}} = \{x_{l,\pi(i)}^{(1)} : x_{l,i}^{(1)} \in v_{l,1}, y_i = y_{\pi(i)}\} \quad (1)$$

Now, $\widetilde{v_{l,1}}$ is a permutation of $v_{l,1}$ where the original image differs, but the ground-truth class remains the same. Through this permutation, we augment the size of the possible view pairings, enabling the model to learn richer representations. Regardless of whether the newly permuted pairs are indicative of the positive class (i.e., due to weak labeling), we can still learn invariant features. Note that it was an arbitrary choice to permute $v_{l,1}$, and either view could be permuted without loss of generality.

C. Siamese Architectures

In a Siamese architecture, there are two or three main components depending on the method being used. BYOL consists of an encoder, projector, and predictor, while SimCLR uses only an encoder and projector. We discuss the structure of each component below.

- 1) **Encoder:** ResNet18 [66] feature extractor (i.e., the output of the final average pooling layer), f , producing representation y such that $y = f(v) \in \mathbb{R}^{\mathcal{D}_f}$. We use $\mathcal{D}_f = 512$ in all experiments.
- 2) **Projector:** Multilayer perceptron, g , mapping y to $z = g(y) \in \mathbb{R}^{\mathcal{D}_g}$. We instantiate g as a two-layer multilayer perceptron with a single hidden layer of size 4096 and output size $\mathcal{D}_g = 256$.
- 3) **Predictor:** Multilayer perceptron, q , mapping z to $p = q(z) \in \mathbb{R}^{\mathcal{D}_q}$. We instantiate q as a two-layer multilayer perceptron with a single hidden layer of size 4096 and output size $\mathcal{D}_q = 256$.

Now, we cover how these components are used in both the standard BYOL and SimCLR methods as well as when HistoPerm is added. A high-level overview of our method is shown in Fig. 1.

1) **BYOL:** The BYOL architecture is split across two components called online and target branches, parameterized by θ and ξ , respectively. The online branch is composed of three stages: encoder f_θ , projector g_θ , and predictor q_θ . Likewise, the target branch has two stages: encoder f_ξ and projector g_ξ . Encoders f_θ and f_ξ map input views to a representation space, which are then fed to respective projectors g_θ and g_ξ . Note that the predictor q_θ is only used in the online network, as prior works have shown that this architectural asymmetry is necessary to avoid collapsing to the trivial solution [18]. At the end of training, we only keep the online encoder f_θ and use the pretrained weights as initialization for the fully supervised downstream tasks. Learning progresses by computing the mean squared error between online and target branches. For both unlabeled and labeled views, we compute the loss as follows:

$$\mathcal{L}_{BYOL} = \underbrace{\|q_\theta(z_{u,1}) - sg(z_{u,2})\|}_{Loss_u} + \underbrace{\|q_\theta(\widetilde{z}_{l,1}) - sg(z_{l,2})\|}_{Loss_l} \quad (2)$$

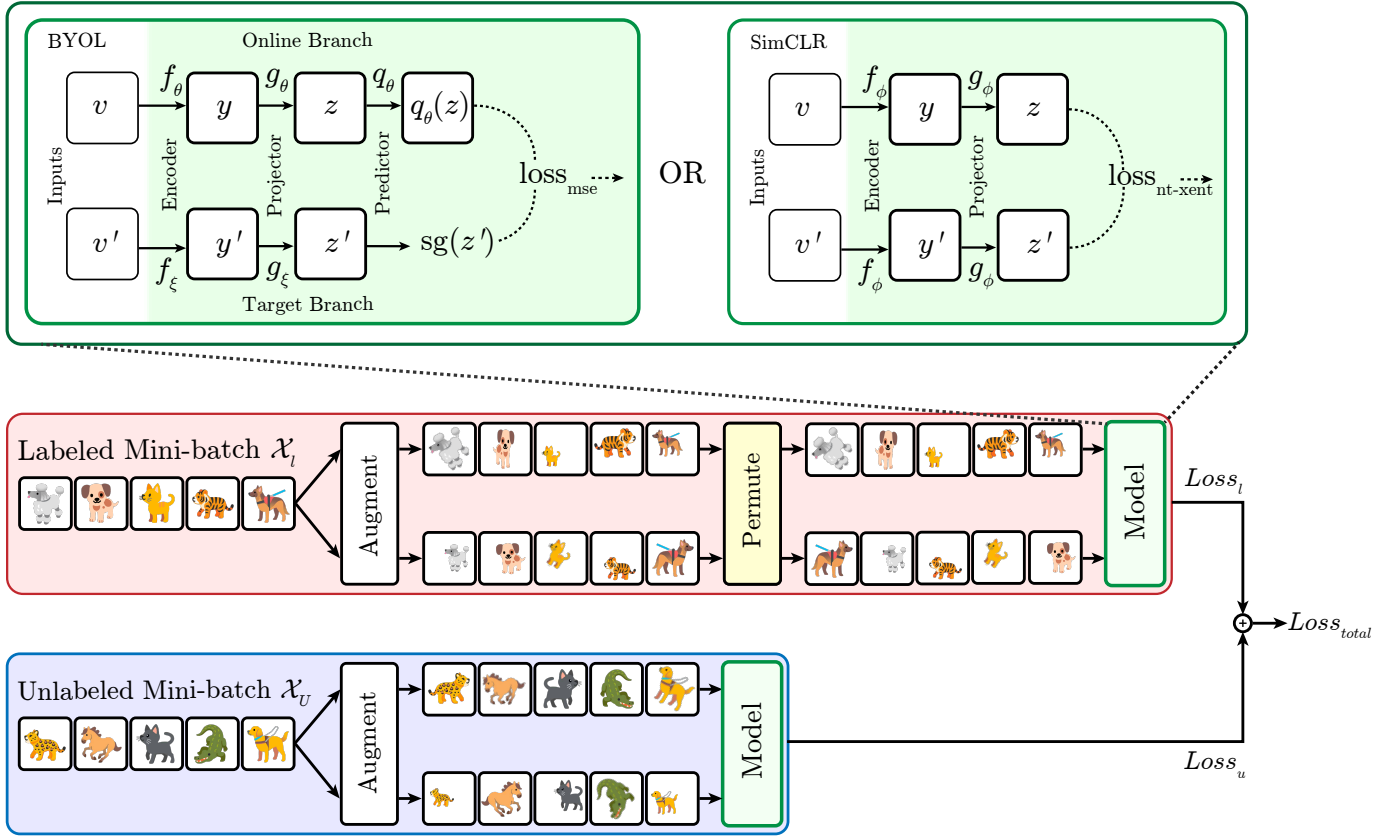


Fig. 1. Overview of our HistoPerm method. The Siamese architectures are fed randomly augmented views v and v' . For the labeled mini-batch \mathcal{X}_l , we show how our method permutes the augmented views before being input to the model. The unlabeled mini-batch \mathcal{X}_u is sent to the network without permutation as in the standard BYOL or SimCLR architectures. For clarity, we use animal pictures in this example, as differences in histology images are difficult to discern for an untrained viewer.

where $\text{sg}(\cdot)$ is the stop-gradient operation, so the target branch weights are not updated through optimization. As shown in the SimSiam paper [18], the stop-gradient is necessary to avoid collapse. We symmetrize the loss by passing $v_{u,2}$, $v_{l,2}$ and $v_{u,1}$, $v_{l,1}$ to the online and target branches, respectively. Although we separate the computation of the forward pass for unlabeled and labeled inputs for (2) in the code implementation, we combine and process both mini-batches simultaneously to avoid inadvertently leaking any information about the source dataset through batch normalization. Note that in the case where $\widetilde{v_{l,1}} = v_{l,2} = \emptyset$ (i.e., $\mathcal{P}_l = \mathcal{X}_l = \emptyset$), our method reduces to the default BYOL formulation.

Then, we perform the weight updates as follows:

$$\theta \leftarrow \text{optimizer}(\theta, \nabla_\theta \mathcal{L}, \eta) \quad (3)$$

$$\xi \leftarrow \tau \xi + (1 - \tau) \xi \quad (4)$$

where $\tau \in [0, 1]$ is a momentum hyperparameter and η is the learning rate for gradient descent.

2) SimCLR: The SimCLR architecture consists of an encoder f_ϕ and projector g_ϕ parameterized by weights ϕ . The encoder f_ϕ maps pairs of input views to representations that are then fed to the projector g_ϕ . Finally, L_2 -normalization is applied to the outputs of the projector. At the end of training, we only keep the encoder f_ϕ and use the pretrained weights as initialization for the fully supervised downstream tasks.

Learning progresses using the NT-Xent loss as defined in the original SimCLR formulation [16]. For both unlabeled and labeled views, we compute the loss as follows:

$$\begin{aligned} \mathcal{L}_{SimCLR} = & \frac{1}{|\mathcal{X}_u| + |\mathcal{X}_l|} \left[\sum_{i=1}^{|\mathcal{X}_u|} -\log \underbrace{\frac{\exp(z_i \cdot z'_i / \tau)}{\sum_{k=1}^{|\mathcal{X}_u|+|\mathcal{X}_l|} \exp(z_i \cdot z'_i / \tau)}}_{Loss_u} \right. \\ & \left. + \sum_{i=|\mathcal{X}_u|+1}^{|\mathcal{X}_u|+|\mathcal{X}_l|} -\log \underbrace{\frac{\exp(z_i \cdot z'_i / \tau)}{\sum_{k=1}^{|\mathcal{X}_u|+|\mathcal{X}_l|} \exp(z_i \cdot z'_i / \tau)}}_{Loss_l} \right] \end{aligned} \quad (5)$$

where τ is the temperature hyperparameter. Note that in the case where $\widetilde{v_{l,1}} = v_{l,2} = \emptyset$ (i.e., $\mathcal{P}_l = \mathcal{X}_l = \emptyset$), our method reduces to the default SimCLR formulation.

Then, we perform the weight updates as follows:

$$\phi \leftarrow \text{optimizer}(\phi, \nabla_\phi \mathcal{L}, \eta) \quad (6)$$

where η is the learning rate for gradient descent.

IV. EXPERIMENTAL SETUP

A. Datasets

We applied and evaluated our approach on two publicly available datasets from the Dartmouth-Hitchcock Medical Center (DHMC), a tertiary academic medical center in New Hampshire, USA. Our datasets are representative of Celiac Disease (CD)¹ and Renal Cell Carcinoma (RCC)². Each dataset consists of hematoxylin-eosin-stained, formalin-fixed, paraffin-embedded slides scanned at either $20\times$ (0.5 $\mu\text{m}/\text{pixel}$) or $40\times$ (0.25 $\mu\text{m}/\text{pixel}$) magnification. For run-time efficiency purposes, we downsampled the slides to $5\times$ (2 $\mu\text{m}/\text{pixel}$) magnification using the Lanczos filter [67]. We divided the slides into overlapping 224×224 -pixel patches for easier use with the PyTorch deep learning framework [68]. A different overlapping factor was used across each class in the training set to produce approximately 80,000 patches per class. For the development and testing sets, we used a constant overlap factor of 1.5. We provide dataset distribution statistics in Tables I and II. Please note that, although these datasets are labeled in their original form, we have ignored the labels for a portion of the dataset in each epoch according to the formulation provided in Section III-A to simulate the intended use of our approach. This means that our \mathcal{D}_l and \mathcal{D}_u are varying and built dynamically in each epoch. Note that in our ablation study (Section V-A), we also evaluated our approach using a static, unlabeled dataset for training and measured its effect on the results.

TABLE I

CELIAC DISEASE PATCH-LEVEL DATASET SPLITS FOR THE NORMAL, NON-SPECIFIC DUODENITIS, AND CELIAC SPRUE CLASSES. THE REPORTED GROUND-TRUTH CLASS PER PATCH IS THE CORRESPONDING SLIDE-LEVEL LABEL.

Class	Training	Development	Testing
Normal	81,428	4,535	5,966
Non-specific duodenitis	80,090	9,049	10,010
Celiac sprue	81,560	9,593	10,038

TABLE II

RENAL CELL CARCINOMA PATCH-LEVEL DATASET SPLITS FOR THE BENIGN, ONCOCYTOMA, CHROMOPHOBIC, CLEAR CELL, AND PAPILLARY CLASSES. THE REPORTED GROUND-TRUTH CLASS PER PATCH IS THE CORRESPONDING SLIDE-LEVEL LABEL.

Class	Training	Development	Testing
Benign	80,165	2,231	4,662
Oncocytoma	80,903	1,875	7,895
Chromophobe	80,660	3,672	14,121
Clear cell	78,355	4,701	19,964
Papillary	83,867	2,988	12,625

B. Implementation Details

Image Augmentation: We used a similar set of image augmentations as used in BYOL [15] and SimCLR [16], [17] in our implementation. A patch from each image is randomly selected and resized to 224×224 pixels with bilinear interpolation. Next, unlike the standard set of BYOL and SimCLR data augmentations, we randomly flip the patches over both the horizontal and vertical axes, as histology patches are rotation invariant. Finally, after applying a set of affine transformations (i.e., cropping and flipping), we performed random Gaussian blurring on the augmented images. Empirical justification, as well as exact implementation details for these transformations, are provided in Appendix A.

Pretraining: In the pretraining phase, we used the LARS optimizer [69] for 50 epochs of training the networks with a 5-epoch warm-up and cosine learning rate decay [70] thereafter. The initial learning rate was 0.45 with a mini-batch size of 256 and weight decay of 10^{-6} . The mini-batch was equally split (i.e., 128 examples) between the labeled and unlabeled portions. For the target network in our BYOL experiments, exponential moving average updates were performed with $\tau = 0.97$. For SimCLR, we used the same hyperparameters apart from a learning rate of 0.3 as recommended by the original paper [16].

Linear Evaluation: Linear training uses the SGD optimizer with Nesterov momentum [71] for 80 epochs of training a linear layer on top of the frozen encoder f_θ for BYOL and f_ϕ for SimCLR with a cosine learning rate decay [70]. We used an initial learning rate of 0.2 and a mini-batch size of 256. Unlike the pretraining step, we only performed random affine transformations to the input data. In this phase, we utilized all data in the respective training set.

All experiments were run on either a single NVIDIA Titan RTX, Quadro RTX 8000, or A6000 GPU.

V. RESULTS

To evaluate our method, we compare the results to the standard BYOL and SimCLR architectures, strong noncontrastive and contrastive baselines, respectively. We train the BYOL and SimCLR baselines using the same hyperparameter configuration as enumerated in Section IV-B. To ensure the stability of the results, we report the mean and standard deviation for all metrics across 3 runs with different random seeds.

Linear Evaluation Results: First, we present the results of our model in the linear evaluation mode in Tables III and IV. Overall, models using HistoPerm outperform the corresponding baseline approaches across all datasets. BYOL with HistoPerm outperforms standard BYOL by 8% on CD and 2% on RCC in terms of classification accuracy. Likewise, SimCLR with HistoPerm produces improved accuracy by 3% on CD and 0.25% on RCC.

A. Ablations

We investigated the performance of our model under varying conditions to determine the relative contributions of each component. We performed ablations over the percentage of the mini-batch permuted and unlabeled data scaling.

¹<https://bmirds.github.io/CeliacDisease>

²<https://bmirds.github.io/KidneyCancer>

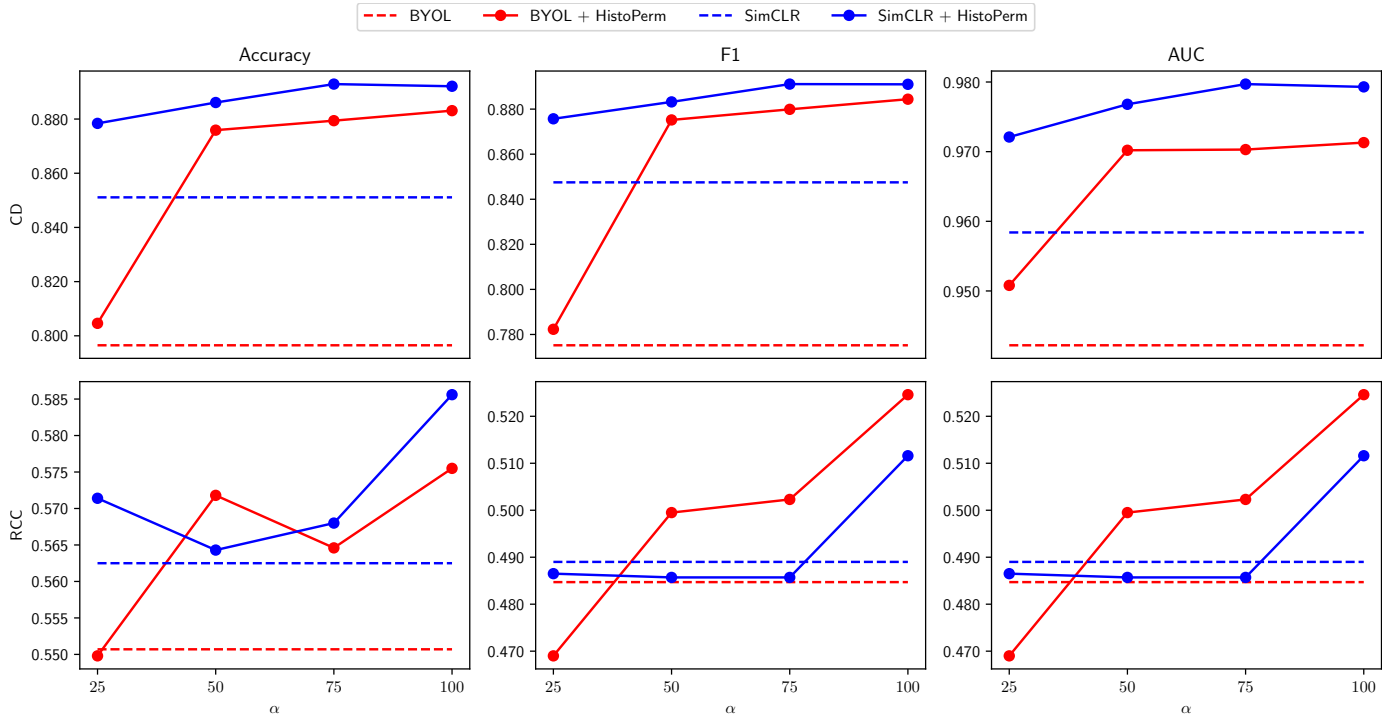


Fig. 2. Ablation results over choices of α , the percentage of the mini-batch used for permutation. We report all results on both test sets.

TABLE III

LINEAR PERFORMANCE RESULTS ON THE CD TEST SET. ALL REPORTED VALUES ARE THE MEAN WITH THE STANDARD DEVIATION ENCLOSED IN PARENTHESES. THE TOP RESULTS FOR EACH ARCHITECTURE ARE PRESENTED IN **BOLDFACE**. WE PROVIDE THE SUPERVISED BASELINE RESULT IN THIS TABLE FOR REFERENCE.

Method	Accuracy	F1	AUC
Supervised	0.6987 (0.0054)	0.6809 (0.0063)	0.8618 (0.0057)
BYOL	0.7965 (0.0212)	0.7752 (0.0294)	0.9422 (0.0101)
BYOL + HistoPerm	0.8759 (0.0114)	0.8752 (0.0113)	0.9702 (0.0055)
SimCLR	0.8511 (0.0023)	0.8475 (0.0030)	0.9584 (0.0014)
SimCLR + HistoPerm	0.8861 (0.0022)	0.8832 (0.0025)	0.9768 (0.0009)

TABLE IV

LINEAR PERFORMANCE RESULTS ON THE RCC TEST SET. ALL REPORTED VALUES ARE THE MEAN WITH THE STANDARD DEVIATION ENCLOSED IN PARENTHESES. THE TOP RESULTS FOR EACH ARCHITECTURE ARE PRESENTED IN **BOLDFACE**. WE PROVIDE THE SUPERVISED BASELINE RESULT IN THIS TABLE FOR REFERENCE.

Method	Accuracy	F1	AUC
Supervised	0.5935 (0.0017)	0.5287 (0.0011)	0.8270 (0.0028)
BYOL	0.5507 (0.0066)	0.4847 (0.0126)	0.8015 (0.0046)
BYOL + HistoPerm	0.5718 (0.0024)	0.4995 (0.0102)	0.8198 (0.0069)
SimCLR	0.5625 (0.0094)	0.4890 (0.0046)	0.8151 (0.0050)
SimCLR + HistoPerm	0.5643 (0.0054)	0.4857 (0.0039)	0.8213 (0.0141)

Mini-batch permutation percentage: To understand the effects of our view permutation method, we reframe this problem as permuting a certain percentage of the input mini-batch. Specifically, we seek to determine the effects of no permutation up to 100% permutation of the mini-batch with other intermediate values tested. Of note, the 0% permutation is equivalent to the standard BYOL and SimCLR methods, as all elements of the mini-batch are considered unlabeled.

Likewise, 50% permutation is equivalent to HistoPerm, as only half of the elements of a mini-batch are considered unlabeled. We denote the percentage of the mini-batch eligible for permutation as α . We present our results in Fig. 2 for the linear evaluation mode on the respective test sets.

From our ablations over α , we conclude that selecting $\alpha = 50\%$ (i.e., the equivalent of the default setting for the HistoPerm method) is a good choice for most datasets, as in all cases, it outperforms the standard methods in terms of accuracy. However, more performance could be obtained by fine-tuning α in certain scenarios, as evidenced by the directly related increase in α and classification performance on the RCC dataset. We find that any value of α results in improved performance over the respective baseline methods in terms of accuracy, indicating that all permutation choices should provide a measurable improvement. However, using a larger value of α requires more labeled data, so it is still critical to find a balance between the labeled dataset size and accuracy. Understandably, we observe that in general, our model performance increases along with α due to the larger set of unique views available for permutation. We anticipate that this trend will continue with larger mini-batch sizes as well. Last, even suboptimal values of α produce promising results, so expensive fine-tuning on this hyperparameter may not be necessary in most cases.

Unlabeled data: We explored the effects of adding additional data from a larger CD dataset, which is a superset of the dataset introduced in Section IV-A. The additional data consist of approximately 320,000 patches in addition to the existing $\sim 240,000$ patches in our original CD dataset. We denote this unlabeled addendum to the CD dataset as CD_u . According to the formulation from Section III-B, the original CD and new

TABLE V

LINEAR EVALUATION MODE RESULTS FOR THE ABLATION STUDY USING UNLABELED DATA. THE TOP RESULTS FOR EACH ARCHITECTURE ARE PRESENTED IN **BOLDFACE**.

Method	CD			CD + CD _u		
	Accuracy	F1	AUC	Accuracy	F1	AUC
BYOL	0.7965 (0.0212)	0.7752 (0.0294)	0.9422 (0.0101)	0.8454 (0.0046)	0.8400 (0.0056)	0.9558 (0.0030)
BYOL + HistoPerm	0.8759 (0.0114)	0.8752 (0.0113)	0.9702 (0.0055)	0.8837 (0.0071)	0.8860 (0.0078)	0.9713 (0.0026)
SimCLR	0.8511 (0.0023)	0.8475 (0.0030)	0.9584 (0.0014)	0.8793 (0.0091)	0.8799 (0.0074)	0.9690 (0.0010)
SimCLR + HistoPerm	0.8861 (0.0022)	0.8832 (0.0025)	0.9768 (0.0009)	0.8971 (0.0088)	0.8928 (0.0103)	0.9790 (0.0012)

CD_u datasets represent \mathcal{P}_l and \mathcal{P}_u after conversion to patches, respectively. To simulate the impact of adding more unlabeled data, we ignore any existing labels for CD_u. For reference, we provide the distribution of labels in Appendix B, although they were not used during the training. Note that CD \cap CD_u = \emptyset . We present our results in the linear evaluation mode with the addition of CD_u in Table V.

We found that BYOL and SimCLR were improved by 5% and 2%, respectively, with the addition of the unlabeled data. Given that histology images are expensive to annotate, it is plausible that HistoPerm could be used as a viable alternative to tedious manual labeling across the entire dataset and that only a subset would require labeling. Of note, the CD_u dataset primarily consists of “Normal” slides, meaning typically imbalanced histology data distributions should not pose a problem for HistoPerm. Moreover, these results indicate that HistoPerm still produces a notable performance gain despite having access to only a fixed labeled subset.

VI. DISCUSSION

In this paper, we introduced HistoPerm, a new permutation-based view generation method for representation learning tailored for histology images. Our experimental results demonstrate that adding HistoPerm to BYOL and SimCLR significantly improves classification accuracy on two public histology datasets. These results are important, as they show that HistoPerm can achieve measurably higher accuracy than established competing methods while incurring no additional computational cost. Moreover, HistoPerm can even outperform the supervised baseline in some cases while using less labeled data. Given that histology image annotation is a tedious and highly skilled process, reducing the labeling burden could have a notable impact on the utility of the approach in clinical applications.

Notably, we showed that adding HistoPerm can even outperform the corresponding supervised baseline by a sizable margin on the CD dataset. However, this trend did not hold on the RCC dataset, where all representation learning models performed worse than the supervised baseline. Moreover, the results on the RCC dataset did not display as measurable of an improvement as the respective CD experiments. We hypothesize that this discrepancy is due to the increased morphological complexity and atypicality of the RCC samples, as noted by the authors in the original dataset paper [1]. Despite the smaller performance improvements on RCC, adding HistoPerm on both datasets provides a clear benefit over existing representation learning approaches. In future

work, we intend to delve deeper into the relationships between histologic subtype complexity and model performance to aid the model in producing more representative features.

HistoPerm leverages the weakly labeled nature of histology images to expand the available pool of views for representation learning. We showed that the expanded set of candidate views is essential for producing better representations and results in improved downstream performance. As shown in the ablation study in Section V-A, increasing α (i.e., the number of views eligible for permutation) produces higher classification accuracy in linear evaluation mode. These results indicate the additional scaling possible with the use of more labeled data. However, even models using less labeled data (i.e., smaller value of α) perform within 1 – 2% in most cases, indicating that performance saturates. Using this observation, practitioners applying HistoPerm can make reasonable tradeoffs between final performance metrics and data labeling requirements. Furthermore, we demonstrated the effectiveness of HistoPerm on an additional unlabeled dataset and showed that it retained its performance advantage in an intended real-world application.

Despite requiring less labeled data than fully supervised approaches, using HistoPerm still requires some labeled data. Lessening the labeled data burden will allow this approach to be used in low-resource scenarios. In future work, we intend to explore techniques for making our model even more label efficient. Reducing the labeled data requirements would open up HistoPerm to use on more unlabeled datasets that are currently unexplored. In a similar vein, we will explore the impact of adding additional unlabeled data from different sources to verify the generalizability of HistoPerm across histology datasets with varying preparation and scanning procedures. Moreover, our team plans to incorporate datasets from multiple disease types to examine the effectiveness of the learned representations for histology images in transfer learning. Given that data for certain disease types are rarer and more difficult to obtain, utilizing pretrained representations could provide an avenue for building effective models for diseases with less widely available datasets.

VII. CONCLUSION

This work demonstrated that our new permutation-based view generation method, HistoPerm, provided improved histopathological feature representation and subsequently improved classification performance over existing representation learning approaches. Furthermore, HistoPerm outperformed the supervised baseline model in some scenarios. Our approach

allows for the use of unlabeled histology data alongside labeled data to produce overall higher classification performance. In addition, using HistoPerm will lessen the labeling burden on pathologists, which makes it a more practical approach for various clinical applications.

APPENDIX

A. Data Transformation Hyperparameter Search

We performed a hyperparameter search on the applied image augmentations for use in the pretraining phase. The tested image augmentations are as follows:

- **Cropping:** Randomly sample a patch from the image between 8% and 100% of the original image size (224×224 pixels for our datasets). Additionally, randomly sample an aspect ratio between 3/4 and 4/3. Resize images to 224×224 pixels using bilinear interpolation.
- **Flipping:** Flip the images over the horizontal and vertical axes. Flip over both axes, as histology images are rotation invariant.
- **Color Jittering:** Randomly change the brightness, contrast, hue, and saturation of the image according to a value uniformly selected from a range.
- **Grayscale:** Convert the image to grayscale. Given intensities (r, g, b) for a pixel in the image, convert it to grayscale according to the formula: $0.299r + 0.587g + 0.114b$.
- **Gaussian Blurring:** Use a 23×23 -pixel Gaussian kernel to apply blurring with the standard deviation sampled from the range $[0.1, 2.0]$.
- **Solarization:** Invert all pixels in the image above a threshold.

We use the Kornia computer vision deep learning library for all augmentations [72]. In Table VI, we provide the hyperparameters for the tested data transformations.

TABLE VI

HYPERPARAMETER SETTINGS FOR TESTED DATA TRANSFORMATIONS.

Hyperparameter	\mathcal{T}_1	\mathcal{T}_2
Cropping probability	1.0	1.0
Flipping probability	0.5	0.5
Color jittering		
probability	0.8	0.8
brightness factor	0.4	0.4
contrast factor	0.4	0.4
hue factor	0.1	0.1
saturation factor	0.2	0.2
Grayscale probability	0.2	0.2
Gaussian blurring probability	1.0	0.1
Solarization		
probability	0.0	0.2
threshold	128/255	128/255

Data Transformation Set: We detail the tested data transformation sets as follows:

- **Base:** Apply all transformations as enumerated in Table VI.

- **Remove Grayscale:** Apply all transformations as enumerated in Table VI, apart from random conversion to grayscale.
- **Remove Color:** Apply all transformations as enumerated in Table VI, apart from random conversion to grayscale, color jittering, and solarization.
- **Crop + Blur + Flipping:** Apply cropping, Gaussian blurring, and flipping as enumerated in Table VI.
- **Crop + Flipping:** Apply cropping and flipping as enumerated in Table VI.
- **Blur + Flipping:** Apply Gaussian blurring and flipping as enumerated in Table VI.

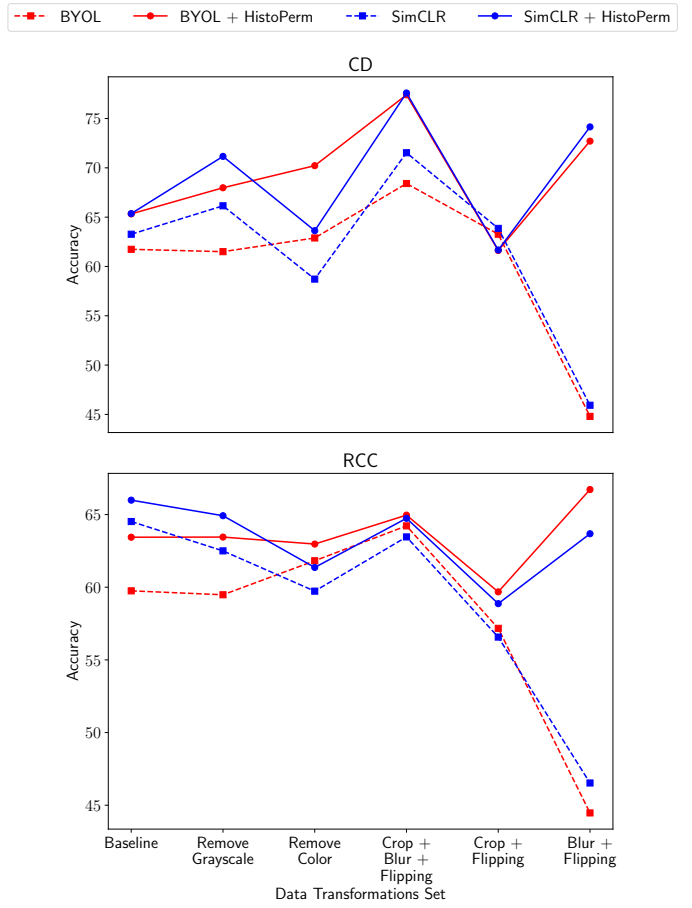


Fig. 3. Linear performance results on the CD and RCC development sets for the tested data transformations.

In Fig. 3, we present the results of our hyperparameter search on the data transformations. Overall, we find that adding HistoPerm provides a measurable classification accuracy improvement in all cases apart from “Crop + Flipping” on the CD dataset. We select “Crop + Blur + Flipping” as the best performing set of data transformations, because it performs well both with and without HistoPerm and should provide the most equitable base for demonstrating the benefits of our approach. Using only “Blur + Flipping” does result in overall higher classification accuracy with HistoPerm, except the results without HistoPerm are significantly lower and are not representative of a baseline model.

B. Unlabeled Dataset CD_u Statistics

In Table VII, we provide the distribution of labels for the unlabeled CD_u dataset as used in Section V-A in the ablation study. As noted in that section, we do not use these labels in the training process, and they are provided solely for the sake of reference.

TABLE VII

ADDITIONAL CELIAC DISEASE PATCH-LEVEL DATASET SPLITS FOR THE NORMAL, NONSPECIFIC DUODENITIS, AND CELIAC SPRUE CLASSES. THE REPORTED PER PATCH LABELS WERE DEDUCED FROM THE CORRESPONDING SLIDE-LEVEL LABELS.

Class	Number of Patches
Normal	280,129
Nonspecific duodenitis	4,525
Celiac sprue	34,613

ACKNOWLEDGMENT

The authors would like to thank Maxwell Aladago, Wayner Barrios, Yiren Jian, Shuai Jiang, Qingyuan Song, and Yuan-sheng Xie for their help and suggestions to improve the manuscript. Additionally, the authors would like to thank Naofumi Tomita for his help and suggestions to improve the manuscript and the figures

REFERENCES

- [1] M. Zhu, B. Ren, R. Richards, M. Suriawinata, N. Tomita, and S. Hassanzpour, “Development and evaluation of a deep neural network for histologic classification of renal cell carcinoma on biopsy and surgical resection slides,” *Sci. Rep.*, vol. 11, p. 7080, 3 2021.
- [2] N. Tomita, B. Abdollahi, J. Wei, B. Ren, A. Suriawinata, and S. Hassanzpour, “Attention-based deep neural networks for detection of cancerous and precancerous esophagus tissue on histopathological slides,” *JAMA Netw. Open*, vol. 2, pp. e1 914 645–e1 914 645, 7 2019.
- [3] J. W. Wei, J. W. Wei, C. R. Jackson, B. Ren, A. A. Suriawinata, and S. Hassanzpour, “Automated detection of celiac disease on duodenal biopsy slides: A deep learning approach,” *J. Path. Inform.*, vol. 10, p. 7, 2019.
- [4] J. W. Wei, L. J. Tafe, Y. A. Linnik, L. J. Vaickus, N. Tomita, and S. Hassanzpour, “Pathologist-level classification of histologic patterns on resected lung adenocarcinoma slides with deep neural networks,” *Sci. Rep.*, vol. 9, p. 3358, 3 2019.
- [5] B. Korbar *et al.*, “Deep learning for classification of colorectal polyps on whole-slide images,” *J. Path. Inform.*, vol. 8, p. 30, 2017.
- [6] S. Jiang, G. J. Zanazzi, and S. Hassanzpour, “Predicting prognosis and idh mutation status for patients with lower-grade gliomas using whole slide images,” *Sci. Rep.*, vol. 11, p. 16849, 2021.
- [7] M. Nasir-Moin *et al.*, “Evaluation of an artificial intelligence–augmented digital system for histologic classification of colorectal polyps,” *JAMA Netw. Open*, vol. 4, pp. e2 135 271–e2 135 271, 11 2021.
- [8] N. Tomita *et al.*, “Predicting oncogene mutations of lung cancer using deep learning and histopathologic features on whole-slide images,” *Translational Oncology*, vol. 24, p. 101494, 10 2022.
- [9] O. Russakovsky, J. Deng, Z. Huang, A. C. Berg, and L. Fei-Fei, “Detecting avocados to zucchinis: what have we done, and where are we going?” in *ICCV*, 2013, pp. 2064–2071.
- [10] B. Bird, K. Bedrossian, N. Laver, M. Miljković, M. J. Romeo, and M. Diem, “Detection of breast micro-metastases in axillary lymph nodes by infrared micro-spectral imaging,” *Analyst*, vol. 134, pp. 1067–1076, 4 2009.
- [11] M. Y. Lu, R. J. Chen, J. Wang, D. Dillon, and F. Mahmood, “Semi-supervised histology classification using deep multiple instance learning and contrastive predictive coding,” 2019. [Online]. Available: <https://arxiv.org/abs/1910.10825>
- [12] B. Li, Y. Li, and K. W. Eliceiri, “Dual-stream multiple instance learning network for whole slide image classification with self-supervised contrastive learning,” in *CVPR*, 2021, pp. 14 318–14 328.
- [13] J. DiPalma, A. A. Suriawinata, L. J. Tafe, L. Torresani, and S. Hassanzpour, “Resolution-based distillation for efficient histology image classification,” *Artif. Intell. Med.*, vol. 119, p. 102136, 2021.
- [14] H. Pinckaers, B. van Ginneken, and G. Litjens, “Streaming convolutional neural networks for end-to-end learning with multi-megapixel images,” *IEEE Trans. Pattern Anal. Mach. Intell.*, vol. 44, pp. 1581–1590, 2022.
- [15] J.-B. Grill *et al.*, “Bootstrap your own latent - a new approach to self-supervised learning,” in *NeurIPS*, H. Larochelle, M. Ranzato, R. Hadsell, M. Balcan, and H. Lin, Eds., vol. 33. Curran Associates, Inc., 2020, pp. 21 271–21 284.
- [16] T. Chen, S. Kornblith, M. Norouzi, and G. Hinton, “A simple framework for contrastive learning of visual representations,” in *ICML*, H. D. III and A. Singh, Eds., vol. 119. PMLR, 7 2020, pp. 1597–1607.
- [17] T. Chen, S. Kornblith, K. Swersky, M. Norouzi, and G. E. Hinton, “Big self-supervised models are strong semi-supervised learners,” in *NeurIPS*, H. Larochelle, M. Ranzato, R. Hadsell, M. Balcan, and H. Lin, Eds., vol. 33. Curran Associates, Inc., 2020, pp. 22 243–22 255.
- [18] X. Chen and K. He, “Exploring simple siamese representation learning,” in *CVPR*, 6 2021, pp. 15 750–15 758.
- [19] K. He, H. Fan, Y. Wu, S. Xie, and R. Girshick, “Momentum contrast for unsupervised visual representation learning,” in *CVPR*, 2020, pp. 9726–9735.
- [20] Y. Tian, C. Sun, B. Poole, D. Krishnan, C. Schmid, and P. Isola, “What makes for good views for contrastive learning?” in *NeurIPS*, H. Larochelle, M. Ranzato, R. Hadsell, M. F. Balcan, and H. Lin, Eds., vol. 33. Curran Associates, Inc., 2020, pp. 6827–6839.
- [21] P. Khosla *et al.*, “Supervised contrastive learning,” in *NeurIPS*, H. Larochelle, M. Ranzato, R. Hadsell, M. Balcan, and H. Lin, Eds., vol. 33. Curran Associates, Inc., 2020, pp. 18 661–18 673.
- [22] A. Deshpande, J. Rock, and D. Forsyth, “Learning large-scale automatic image colorization,” in *ICCV*, 2015, pp. 567–575.
- [23] G. Larsson, M. Maire, and G. Shakhnarovich, “Learning representations for automatic colorization,” in *ECCV*, B. Leibe, J. Matas, N. Sebe, and M. Welling, Eds. Springer International Publishing, 2016, pp. 577–593.
- [24] S. Gidaris, P. Singh, and N. Komodakis, “Unsupervised representation learning by predicting image rotations,” in *ICLR*, 2018.
- [25] Z. Feng, C. Xu, and D. Tao, “Self-supervised representation learning by rotation feature decoupling,” in *CVPR*, 2019, pp. 10 356–10 366.
- [26] M. Noroozi and P. Favaro, “Unsupervised learning of visual representations by solving jigsaw puzzles,” in *ECCV*, B. Leibe, J. Matas, N. Sebe, and M. Welling, Eds. Springer International Publishing, 2016, pp. 69–84.
- [27] M. Noroozi, H. Pirsiavash, and P. Favaro, “Representation learning by learning to count,” in *ICCV*. IEEE Computer Society, 10 2017, pp. 5899–5907.
- [28] X. Chen, H. Fan, R. Girshick, and K. He, “Improved baselines with momentum contrastive learning,” 2020.
- [29] D. Dwibedi, Y. Aytar, J. Tompson, P. Sermanet, and A. Zisserman, “With a little help from my friends: Nearest-neighbor contrastive learning of visual representations,” in *ICCV*, 10 2021, pp. 9588–9597.
- [30] A. van den Oord, Y. Li, and O. Vinyals, “Representation learning with contrastive predictive coding,” 2018. [Online]. Available: <https://arxiv.org/abs/1807.03748>
- [31] O. J. Hénaff *et al.*, “Data-efficient image recognition with contrastive predictive coding,” in *ICML*. arXiv, 2020, pp. 4182–4192.
- [32] M. Caron, P. Bojanowski, A. Joulin, and M. Douze, “Deep clustering for unsupervised learning of visual features,” in *ECCV*, 9 2018.
- [33] M. Caron, P. Bojanowski, J. Mairal, and A. Joulin, “Unsupervised pre-training of image features on non-curated data,” in *ICCV*. IEEE Computer Society, 10 2019, pp. 2959–2968.
- [34] M. Caron, I. Misra, J. Mairal, P. Goyal, P. Bojanowski, and A. Joulin, “Unsupervised learning of visual features by contrasting cluster assignments,” in *NeurIPS*, H. Larochelle, M. Ranzato, R. Hadsell, M. Balcan, and H. Lin, Eds., vol. 33. Curran Associates, Inc., 2020, pp. 9912–9924.
- [35] M. Azabou *et al.*, “Mine your own view: Self-supervised learning through across-sample prediction,” 2021.
- [36] J. Zbontar, L. Jing, I. Misra, Y. LeCun, and S. Deny, “Barlow twins: Self-supervised learning via redundancy reduction,” in *ICML*, M. Meila and T. Zhang, Eds. PMLR, 7 2021, pp. 12 310–12 320.
- [37] A. Ermolov, A. Siarohin, E. Sangineto, and N. Sebe, “Whitening for self-supervised representation learning,” in *ICML*, M. Meila and T. Zhang, Eds., vol. 139. PMLR, 7 2020, pp. 3015–3024.

[38] A. Bardes, J. Ponce, and Y. LeCun, "Vicreg: Variance-invariance-covariance regularization for self-supervised learning," in *ICLR*, 2022. [Online]. Available: <https://openreview.net/forum?id=xm6YD62D1Ub>

[39] P. H. Richemond *et al.*, "Byol works even without batch statistics," 2020. [Online]. Available: <https://arxiv.org/abs/2010.10241>

[40] A. Fetterman and J. Albrecht, "Understanding self-supervised and contrastive learning with "bootstrap your own latent" (byol)," 8 2020. [Online]. Available: <https://untitled-ai.github.io/understanding-self-supervised-contrastive-learning.html>

[41] Y. Liu *et al.*, "Detecting cancer metastases on gigapixel pathology images," 2017. [Online]. Available: <https://arxiv.org/abs/1703.02442>

[42] Z. Swiderska-Chadaj *et al.*, "A deep learning approach to assess the predominant tumor growth pattern in whole-slide images of lung adenocarcinoma," in *Medical Imaging 2020: Digital Pathology*, J. E. Tomaszewski and A. D. Ward, Eds., vol. 11320. SPIE, 2020, pp. 84–91.

[43] S. Graham, M. Shaban, T. Qaiser, N. A. Koohbanani, S. A. Khurram, and N. Rajpoot, "Classification of lung cancer histology images using patch-level summary statistics," in *Medical Imaging 2018: Digital Pathology*, J. E. Tomaszewski and M. N. Gurcan, Eds., vol. 10581. SPIE, 2018, pp. 327–334.

[44] A. Cruz-Roa *et al.*, "Automatic detection of invasive ductal carcinoma in whole slide images with convolutional neural networks," in *Medical Imaging 2014: Digital Pathology*, M. N. Gurcan and A. Madabhushi, Eds., vol. 9041. SPIE, 3 2014, pp. 1–15.

[45] A. BenTaieb and G. Hamarneh, "Predicting cancer with a recurrent visual attention model for histopathology images," in *MICCAI*, A. F. Frangi, J. A. Schnabel, C. Davatzikos, C. Alberola-López, and G. Fichtinger, Eds. Springer International Publishing, 2018, pp. 129–137.

[46] M. Ilse, J. Tomczak, and M. Welling, "Attention-based deep multiple instance learning," in *ICML*, J. Dy and A. Krause, Eds., vol. 80. PMLR, 7 2018, pp. 2127–2136.

[47] M. Lerousseau *et al.*, "Weakly supervised multiple instance learning histopathological tumor segmentation," in *MICCAI 2020*, A. L. Martel *et al.*, Eds. Springer International Publishing, 2020, pp. 470–479.

[48] C. Mercan, S. Aksoy, E. Mercan, L. G. Shapiro, D. L. Weaver, and J. G. Elmore, "Multi-instance multi-label learning for multi-class classification of whole slide breast histopathology images," *IEEE Trans. Med. Imag.*, vol. 37, pp. 316–325, 1 2018.

[49] A. Patil, D. Tamboli, S. Meena, D. Anand, and A. Sethi, "Breast cancer histopathology image classification and localization using multiple instance learning," in *WIECON-ECE*, 2019, pp. 1–4.

[50] G. Campanella *et al.*, "Clinical-grade computational pathology using weakly supervised deep learning on whole slide images," *Nat. Med.*, vol. 25, pp. 1301–1309, 8 2019.

[51] Y. Zhao *et al.*, "Predicting lymph node metastasis using histopathological images based on multiple instance learning with deep graph convolution," in *CVPR*, 2020, pp. 4836–4845.

[52] A. Katharopoulos and F. Fleuret, "Processing megapixel images with deep attention-sampling models," in *ICML*, K. Chaudhuri and R. Salakhutdinov, Eds., vol. 97. PMLR, 7 2019, pp. 3282–3291.

[53] A. Tarkhan, T. K. Nguyen, N. Simon, T. Bengtsson, P. Ocampo, and J. Dai, "Attention-based deep multiple instance learning with adaptive instance sampling," in *ISBI*, 2022, pp. 1–5.

[54] P. Chikontwe, M. Kim, S. J. Nam, H. Go, and S. H. Park, "Multiple instance learning with center embeddings for histopathology classification," in *MICCAI*, A. L. Martel *et al.*, Eds. Springer International Publishing, 2020, pp. 519–528.

[55] N. A. Koohbanani, B. Unnikrishnan, S. A. Khurram, P. Krishnaswamy, and N. Rajpoot, "Self-path: Self-supervision for classification of pathology images with limited annotations," *IEEE Trans. Med. Imag.*, vol. 40, pp. 2845–2856, 2021.

[56] M. Sahasrabudhe *et al.*, "Self-supervised nuclei segmentation in histopathological images using attention," in *MICCAI*, A. L. Martel *et al.*, Eds. Springer International Publishing, 2020, pp. 393–402.

[57] R. J. Chen and R. G. Krishnan, "Self-supervised vision transformers learn visual concepts in histopathology," *Learning Meaningful Representations of Life, NeurIPS*, 2021.

[58] Q. D. Vu, K. Rajpoot, S. E. A. Raza, and N. Rajpoot, "Handcrafted histological transformer (h2t): Unsupervised representation of whole slide images," 2022. [Online]. Available: <https://arxiv.org/abs/2202.07001>

[59] C. L. Srinidhi and A. L. Martel, "Improving self-supervised learning with hardness-aware dynamic curriculum learning: An application to digital pathology," in *ICCVW*. IEEE Computer Society, 10 2021, pp. 562–571.

[60] K. Stacke, J. Unger, C. Lundström, and G. Eilertsen, "Learning representations with contrastive self-supervised learning for histopathology applications," 2021. [Online]. Available: <https://arxiv.org/abs/2112.05760>

[61] O. Dehaene, A. Camara, O. Moindrot, A. de Lavergne, and P. Courtiol, "Self-supervision closes the gap between weak and strong supervision in histology," 2020. [Online]. Available: <https://arxiv.org/abs/2012.03583>

[62] K. Stacke, C. Lundström, J. Unger, and G. Eilertsen, "Evaluation of contrastive predictive coding for histopathology applications," in *ML4H NeurIPS Workshop*, E. Alsentzer, M. B. A. McDermott, F. Falck, S. K. Sarkar, S. Roy, and S. L. Hyland, Eds., vol. 136. PMLR, 7 2020, pp. 328–340.

[63] O. Ciga, T. Xu, and A. L. Martel, "Self supervised contrastive learning for digital histopathology," *Machine Learning with Applications*, vol. 7, p. 100198, 2022.

[64] J. Ke, Y. Shen, X. Liang, and D. Shen, "Contrastive learning based stain normalization across multiple tumor in histopathology," in *MICCAI*, M. de Bruijne *et al.*, Eds. Springer International Publishing, 2021, pp. 571–580.

[65] J. Gildenblat and E. Klaiman, "Self-supervised similarity learning for digital pathology," in *MICCAI COMPAY Workshop*. arXiv, 2019. [Online]. Available: <https://arxiv.org/abs/1905.08139>

[66] K. He, X. Zhang, S. Ren, and J. Sun, "Deep residual learning for image recognition," in *CVPR*, 2015, pp. 770–778.

[67] K. Turkowski, *Filters for Common Resampling Tasks*. Academic Press Professional, Inc., 1990.

[68] A. Paszke *et al.*, "Pytorch: An imperative style, high-performance deep learning library," in *NeurIPS*, H. Wallach, H. Larochelle, A. Beygelzimer, F. d Alché-Buc, E. Fox, and R. Garnett, Eds. Curran Associates, Inc., 2019, pp. 8024–8035.

[69] Y. You, I. Gitman, and B. Ginsburg, "Large batch training of convolutional networks," 2017. [Online]. Available: <https://arxiv.org/abs/1708.03888>

[70] I. Loshchilov and F. Hutter, "Sgdr: Stochastic gradient descent with warm restarts," in *ICLR*, 2017.

[71] I. Sutskever, J. Martens, G. Dahl, and G. Hinton, "On the importance of initialization and momentum in deep learning," in *ICML*, S. Dasgupta and D. McAllester, Eds., vol. 28. PMLR, 7 2013, pp. 1139–1147.

[72] E. Riba, D. Mishkin, D. Ponsa, E. Rublee, and G. Bradski, "Kornia: an open source differentiable computer vision library for pytorch," in *Proc. IEEE/CVF Winter Conf. Appl. Comput. Vis. (WACV)*, 2020.